

Article

Ethanol- and Methanol-Coordinated and Solvent-Free Dodecahydro *closo*-Dodecaborates of 3*d* Transition Metals and of Magnesium

Emilie Didelot ¹, Zbigniew Łodziana ² , Fabrizio Murgia ¹ and Radovan Černý ^{1,*}

¹ Department of Quantum Matter Physics, Laboratory of Crystallography, University of Geneva, Quai Ernest Ansermet 24, CH-1211 Geneva, Switzerland

² Polish Academy of Sciences, Institute of Nuclear Physics, ul. Radzikowskiego 152, 31-342 Kraków, Poland

* Correspondence: Radovan.Cerny@unige.ch

Received: 25 June 2019; Accepted: 19 July 2019; Published: 21 July 2019



Abstract: Magnesium and 3*d* transition metals *closo*-borates were prepared by mechanosynthesis (ball milling) of the mixtures Na₂B₁₂H₁₂ + MCl₂ (M = Mn, Fe, Co, Ni, Mg), followed by addition of ethanol or methanol and drying under dynamic vacuum. The dead mass of NaCl is partly removed by filtration. The crystal structures of solvent-coordinated and solvent-free *closo*-borates have been characterized by temperature dependent synchrotron radiation X-ray powder diffraction, ab initio calculations, thermal analysis and infrared spectroscopy. Various solvated complexes containing six, four, three, two or one solvent molecules were obtained by successive removal of the solvent until in most case the solvent-free metal *closo*-borates were obtained with the exception of Mg whose hypothetical crystal structure, however, could have its prototype in MnB₁₂H₁₂. The 3*d* transition metal *closo*-borates were studied in the view of their potential use as Na- or Li-ion battery electrodes in combination with Na or Li *closo*-borate solid electrolytes. The metal oxidation state (II) obtained in compounds presented here does not allow such application.

Keywords: *Closo*-borate; transition metal; ethanol complex; methanol complex; X-ray powder diffraction

1. Introduction

Dodecahydro *closo*-dodecaborates of transition metals (TM) have attracted interest for various applications [1,2], and have been studied in the framework of boron chemistry. As most of the compounds have been crystallized from solution they are very often prepared in solvated state [3–12].

Our interest in TM *closo*-borates started with studies of *closo*-borates as solid electrolytes [13–19]. The TM *closo*-borates were considered as materials for electrodes in Li- and Na-ion solid-state batteries thus providing chemical compatibility of electrode/electrolyte interface. We have recently reported a method of nickel *closo*-borate synthesis by mechanochemistry from precursors Na₂B₁₂H₁₂ and NiCl₂ followed by hydration, crystallization and drying [20]. The precursor Na₂B₁₂H₁₂ is usually prepared by synthetic routes involving toxic B₂H₆, or expensive B₁₀H₁₄ [9]. As an alternative, there exists a method of Na₂B₁₂H₁₂ synthesis from non-toxic and cheap NaBH₄ [21]. We have then applied the synthetic method to *closo*-borates of 3*d* transition metals and of magnesium using water as a solvent [22]. Only a low oxidation state (II) of the TMs has been stabilized in these compounds, which are therefore not applicable as insertion electrodes. In this manuscript, we report on *closo*-borates of 3*d* transition metals and of magnesium synthesized using ethanol (EtOH) or methanol (MeOH) as a solvent. We show that the oxidation state of TMs is (II), and that a removal of coordinating solvent molecules by drying is an easy way of preparing the solvent-free *closo*-borates for most 3*d* TMs.

2. Materials and Methods

2.1. Synthesis

The precursors MnCl_2 , FeCl_2 , CoCl_2 , NiCl_2 and MgCl_2 (98%, Aldrich) and $\text{Na}_2\text{B}_{12}\text{H}_{12}$ (99.5%, Katchem) were used as purchased. The samples were prepared by ball-milling the mixtures



in a Fritsch Pulverisette 7 planetary mill, under Argon atmosphere. The ball-to-mass ration was approximately 1:50. The mixtures were milled for a total time of 1 h (2 min of ball-milling and 2 min break, 15 repetitions) with a speed of 100 rpm. After the ball-milling, the solvent (ethanol—absolute, analytical Reagent grade, >99.8% and methanol—analytical reagent grade, >99.9%, Fischer Chemicals) was added to the samples and heated to 110 °C for ethanol and 90 °C for methanol. The resulting NaCl could be removed by dissolution of *closo*-borate in ethanol, filtration, and drying at 110 °C. All manipulations of the samples were performed in a glove box, under Argon atmosphere.

2.2. Synchrotron Radiation X-Ray Powder Diffraction (SR-XPD)

The data used for crystal structure and refinements were collected at the Swiss Norwegian Beamlines of ESRF (European Synchrotron Radiation Facility, Grenoble, France) between 25 and 400 °C (T-ramps). SR-XPD were recorded on Dectris Pilatus M2 detector at wavelengths of 0.69425, 0.7225, 0.77936, 0.7849 or 0.8187 Å calibrated with NIST SRM640c Si standard. The 2D images were integrated and treated with the locally written program Bubble.

For all measurements, the samples were sealed into borosilicate capillaries of diameter 0.5 mm (under argon atmosphere), which were spun during data acquisition, and the temperature was controlled with a hot air blower calibrated with silver thermal dilatation. The dynamical vacuum was used to eliminate the solvent molecules in the capillaries during the measurement contrary to the measurements labelled as “closed system” where the capillaries were only heated. Crystal structures were solved ab-initio using the software FOX [23] and refined with the Rietveld method using TOPAS [24]. *Closo*-borate anion $\text{B}_{12}\text{H}_{12}^{2-}$ was modelled as rigid body with ideal icosahedral shape and with corresponding B-H and B-B distances. The interatomic distances and coordination polyhedra were analyzed using programs DIAMOND [25] and PLATON [26].

2.3. Fourier Transform Infrared Spectroscopy (FTIR)

FTIR experiments were performed using a Bio-Rad Excalibur Instrument between 600 and 4000 cm^{-1} with a spectral resolution set to 1 cm^{-1} .

2.4. Differential Scanning Calorimetry (DSC) and Thermogravimetry (TG)

DSC/TG data were measured using a NETZCH STA449 F3 Jupiter instrument from 30 °C to 350 °C. The measurements were performed under inert atmosphere of nitrogen with a purge rate of 20 mL/min. The sample were contained in sealed Al crucibles which were drilled before closing the DSC to allow solvent molecules to escape during the heating. The heating rate was 10 °C/min. Approximately 2 mg of sample was used for each run.

2.5. Ab Initio Calculations

In order to gain some insight into charge distribution within EtOH or MeOH coordinated and solvent free samples; also to determine hydrogen atoms positions and confirm the crystal structures density functional theory (DFT) calculations were performed within the spin polarized plane wave DFT method implemented in Vienna ab initio Simulation Package (VASP) [27]. The atoms were replaced with projected augmented wave potentials [28] with the valence electron configurations ($1s^1$) for H, ($2s^2 2p^1$) for B, ($2s^2 2p^4$) for O, ($3d^8 4s^2$) for Ni, ($3d^8 4s^1$) for Co, ($3d^7 4s^1$) for Fe, ($3s^2$) for Mg and ($3d^6 4s^1$)

for Mn. The gradient-corrected (GGA) exchange-correlation functional and the non-local correction accounting for a weak dispersive interactions were applied [29,30]. In order to account for strong correlation effects in the valence orbitals of transition metals the GGA+U method was used with Hubbard $U = 5.0$ eV [31]. We have assumed antiferromagnetic ordering for all crystalline structures. Detailed analysis of the magnetic properties are beyond the scope of the present study.

For each crystal structure atomic positions were relaxed according to conjugated gradient (CG) algorithm. The lattice parameters were not optimized, and they were frozen at experimental values. For configurations with partial occupancies we have constructed at least two independent configurations with all sites fully occupied. Each of these structures was independently optimized and the one with lower ground state energy was used for structural analysis and charge density analysis. The later was performed with Bader method [32]. In order to improve the accuracy the charge density sampling grid was doubled for the charge analysis.

3. Results

3.1. Phase Analysis by SR-XPD and DSC/TG

The thermal stability and quantitative phase composition were investigated by SR-XPD and DSC/TG. Selected DSC/TG curves are shown in Figures 1 and 2. As already discussed in [20,22] the temperature-dependent phase evolution is influenced by the gas pressure in the sample container. While the calorimetry was performed in an open crucible under nitrogen flow, the SR-XPD data were collected in a closed system or under dynamic vacuum using glass capillaries. The difference in experimental conditions lead to discrepancies observed between DSC/TG and SR-XPD experiments.

All crystal structures were solved ab initio from SR-XPD data, followed by the assignment of structure types. Selected representatives for each structure type were validated by DFT calculations. Space groups (corroborated by DFT calculations) and experimental lattice parameters are summarized in Table 1. Diffraction data at variable temperature are shown for the cobalt (Figures 3 and 4) sample. Remaining data can be found in the Supplementary Materials, along with Rietveld plots. The CIF files obtained from Rietveld refinement and those from DFT calculations have been deposited to the ICSD (See Supplementary Materials Figures S1–S37).

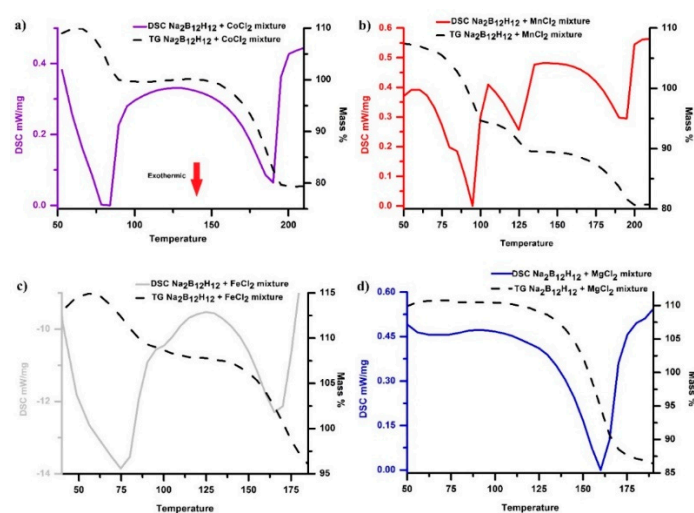


Figure 1. Differential scanning calorimetry (DSC)/thermogravimetry (TG) heating curves for ball-milled and solvated with ethanol (a) $\text{Na}_2\text{B}_{12}\text{H}_{12} + \text{CoCl}_2$, (b) $\text{Na}_2\text{B}_{12}\text{H}_{12} + \text{MnCl}_2$, (c) $\text{Na}_2\text{B}_{12}\text{H}_{12} + \text{FeCl}_2$ and (d) $\text{Na}_2\text{B}_{12}\text{H}_{12} + \text{MgCl}_2$ mixtures. The samples were loaded in an open crucible to allow the removal of ethanol molecules. The samples were shortly exposed to air during the loading in the instrument, and adsorbed the humidity. This explains the starting TG values higher than 100%.

The phase evolution of as prepared samples with temperature as observed by SR-XPD under dynamic vacuum and in closed system is schematically shown in Figure 5. In the following, we discuss the crystalline phase evolution in dried samples, the corresponding crystal structures are presented in Section 3.2.

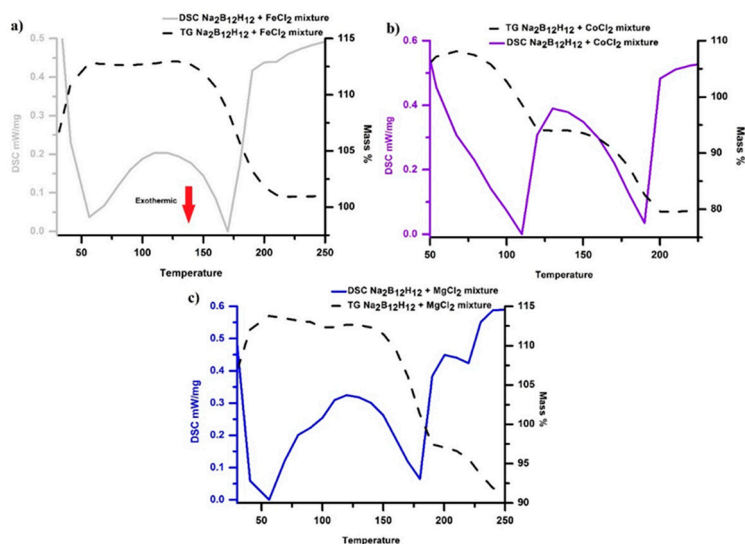


Figure 2. DSC/TG heating curves for ball-milled and solvated with methanol (a) $\text{Na}_2\text{B}_{12}\text{H}_{12} + \text{FeCl}_2$, (b) $\text{Na}_2\text{B}_{12}\text{H}_{12} + \text{CoCl}_2$ and (c) $\text{Na}_2\text{B}_{12}\text{H}_{12} + \text{MgCl}_2$ mixtures. The samples were loaded in an open crucible to allow the removal of methanol molecules. The samples were shortly exposed to air during the loading in the instrument, and adsorbed the humidity. This explains the starting TG values higher than 100%.

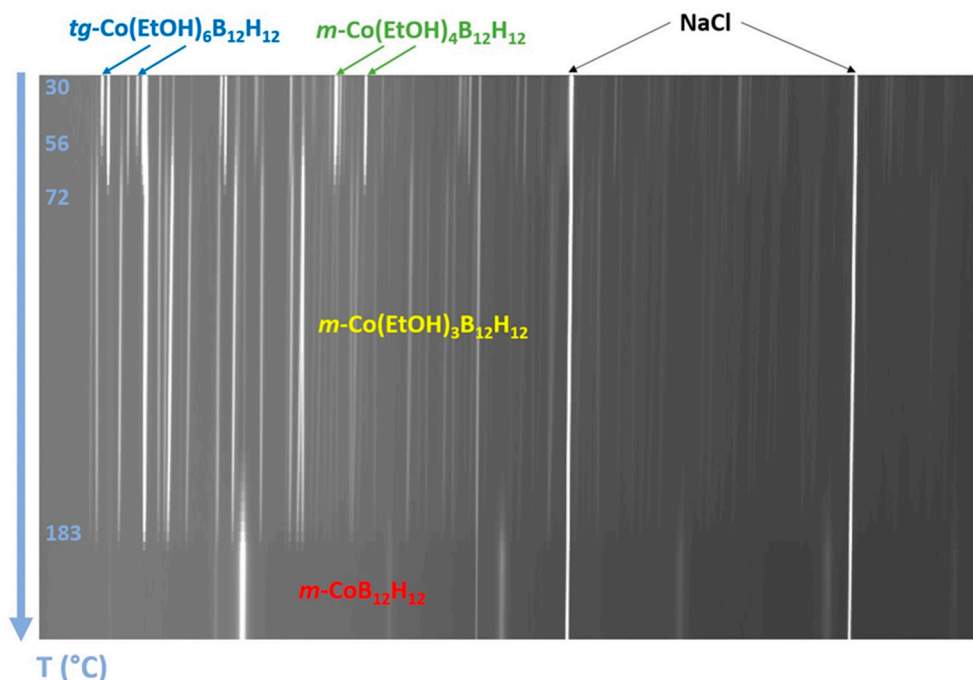


Figure 3. Temperature dependent X-ray powder diffraction patterns (T-ramp) for ball-milled $\text{Na}_2\text{B}_{12}\text{H}_{12} + \text{CoCl}_2$ mixture loaded with ethanol (heating rate 6 K/min under dynamic vacuum, $\lambda = 0.69425 \text{ \AA}$).

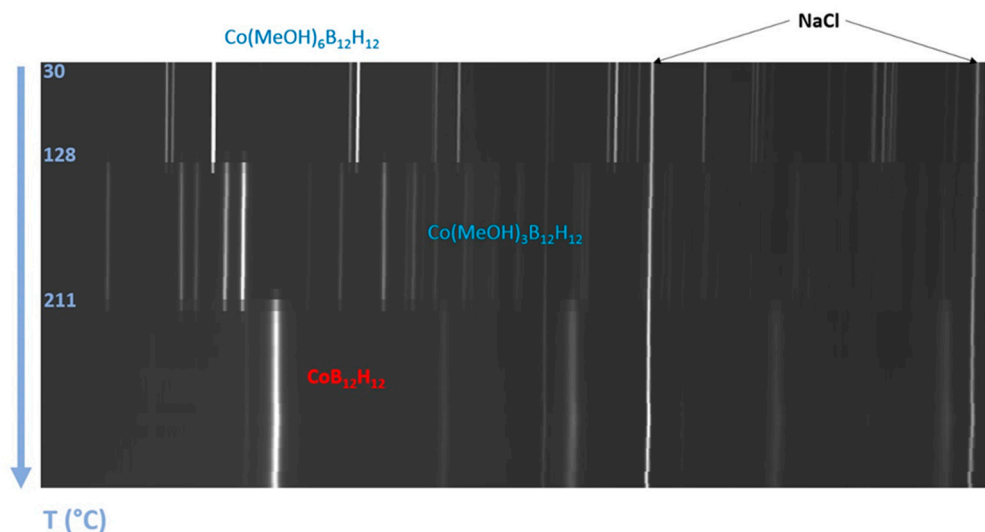


Figure 4. Temperature dependent X-ray powder diffraction patterns (T-ramp) for ball-milled $\text{Na}_2\text{B}_{12}\text{H}_{12}$ + CoCl_2 mixture loaded with methanol (heating rate 10 K/min under dynamic vacuum, $\lambda = 0.77936 \text{ \AA}$).

In all studied systems, i.e., EtOH and MeOH syntheses with all metals, the phase observed in as prepared samples is the complex with six ligands. The presence of this complex in the systems Fe-EtOH and Ni-EtOH is not proved by structural analysis, but is very probable as the phases formed by thermolysis of as prepared samples contain less than six ligands. The phase obtained by the thermolysis of hexa-complex in EtOH systems is usually a complex with four ligands. The Mn-EtOH system is an exception where the tetra-complex is not observed, and in some systems it may be present as an unknown phase. The next phase obtained by the thermolysis is the three ligands complex, which is formed in both, EtOH and MeOH syntheses. In some systems, the synthesized sample contains two or three phases, i.e., the complexes with six, four and three ligands. The co-existence of the complexes in as prepared samples is explained by different solvation rates, as the amount of added solvent is not precisely measured. In the systems with Mn and Fe the successive removal of ligands by thermolysis proceed further, and the complexes with two and one ligands are formed. The mono-complex in Mn-EtOH system contains also one molecule of EtOH that does not coordinate the metal.

The unsolvated metal closo-borates have been obtained only for Mn-EtOH, Fe-MeOH, Ni-MeOH and both Co-systems by further heating under dynamic vacuum. The desolvation was, however, complicated by the reaction with NaCl if the latter was not removed by filtration. It is especially the case of EtOH systems where the formation of Na_6MnCl_8 , Na_6FeCl_8 and $\text{Na}_2\text{Fe}_3\text{Cl}_8$ was observed. The absence of unsolvated $\text{MgB}_{12}\text{H}_{12}$, not formed also in the water assisted synthesis [22], is understood as its instability in a broad interval of temperatures.

The evolution of the phases with temperature differs slightly from the situation in water assisted systems [20,22]. While the first complex formed in all syntheses is always the octahedral hexa-complex, the next complex obtained by the thermolysis is the tetra-complex in water and some EtOH systems, while it is absent in all MeOH assisted systems. The tri-complex is then absent in water assisted syntheses. The crystal structure of the complexes varies with the ligand (see below).

The thermal stability of the complexes depends rather on the ligand than on the metal. While all EtOH complexes are the least stable, the Mn and Fe complexes with MeOH are more stable than those with water, and for Co, Ni and Mg complexes the relation is inversed. The lower stability of EtOH complexes compared with MeOH is surprising comparing the boiling point of EtOH and MeOH. The Mg-complexes are the most stable among all studied metals. One can also note the less rich polymorphism of hexa-complexes with EtOH and MeOH compared to the water. It can be explained by the ratio between ligand size and the size of closo-borate cage as analyzed in [22].

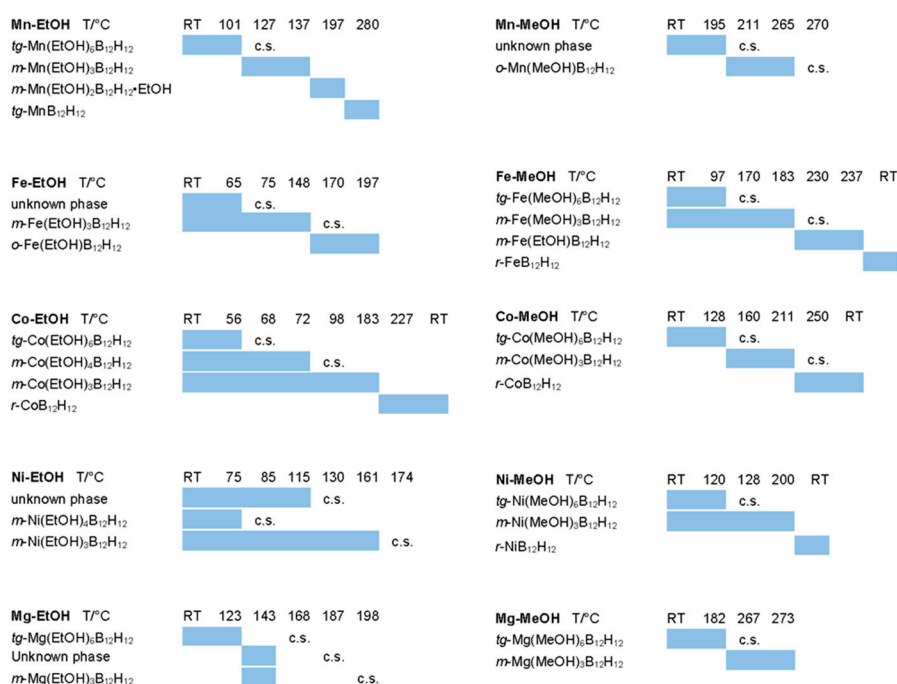


Figure 5. Stability of crystalline compounds observed in metal-EtOH and metal-MeOH samples determined from in-situ X-ray powder diffraction under dynamic vacuum. The phase composition at room temperature (RT) on the left side of the temperature scale corresponds to the as prepared samples. The temperatures of the stability limits in closed system are labelled with c.s.

Table 1. Space group (SG) symmetry, lattice parameters determined at temperature T. The meaning of the prefixes in the compound name are *tg*- for trigonal, *m*- for monoclinic, *o*- for orthorhombic, *r*- for rhombohedral.

Compound	SG	V (Å ³)	a (Å)	b (Å)	c (Å)	β (°)	T (°C)
<i>tg</i> -Mn(EtOH) ₆ B ₁₂ H ₁₂	P31c	1450.61(8)	10.5240(2)		15.1236(5)		30
<i>m</i> -Mn(EtOH) ₃ B ₁₂ H ₁₂	P2 ₁ /n	2005.2(1)	12.0020(4)	11.4436(4)	14.6565(6)	95.051(2)	109
<i>m</i> -Mn(EtOH) ₂ B ₁₂ H ₁₂ •EtOH	P2 ₁ /c	1830.5(7)	11.816(3)	9.035(2)	17.169(4)	92.89(3)	164
<i>tg</i> -MnB ₁₂ H ₁₂	P31c	510.0(1)	7.0679(8)		11.789(1)		212
<i>m</i> -Fe(EtOH) ₃ B ₁₂ H ₁₂	P2 ₁ /n	1979.5(1)	9.3796(3)	18.8924(6)	11.2209(5)	95.422(3)	109
<i>o</i> -Fe(EtOH)B ₁₂ H ₁₂	Pca2 ₁	1278.4(3)	13.805(1)	6.9808(7)	13.265(3)		173
<i>tg</i> -Co(EtOH) ₆ B ₁₂ H ₁₂	P31c	1436.0(2)	10.4762(6)		15.109(1)		40
<i>m</i> -Co(EtOH) ₄ B ₁₂ H ₁₂	P2 ₁	1289.5(1)	9.6630(6)	15.1129(7)	9.6553(6)	113.863(3)	69
<i>m</i> -Co(EtOH) ₃ B ₁₂ H ₁₂	P2 ₁ /n	1954.5(2)	9.3906(4)	18.6357(8)	11.2197(5)	95.491(3)	108
<i>r</i> -CoB ₁₂ H ₁₂	R3	675.5(5)	10.831(3)		6.649(3)		32
<i>m</i> -Ni(EtOH) ₄ B ₁₂ H ₁₂	P2 ₁	1307(1)	9.847(5)	15.048(7)	9.634(4)	113.70(5)	63
<i>m</i> -Ni(EtOH) ₃ B ₁₂ H ₁₂	P2 ₁ /n	1949.1(3)	9.3705(7)	18.625(2)	11.2261(9)	95.814(5)	124
<i>tg</i> -Mg(EtOH) ₆ B ₁₂ H ₁₂	P31c	1434.4(1)	10.4830(4)		15.0717(9)		44
<i>m</i> -Mg(EtOH) ₃ B ₁₂ H ₁₂	P2 ₁ /n	1997.7(2)	9.4535(8)	18.832(1)	11.2693(8)	95.315(4)	143
<i>o</i> -Mn(MeOH)B ₁₂ H ₁₂	Pbca	2482.5(3)	13.497(1)	10.8525(7)	16.948(1)		218
<i>r</i> -Fe(MeOH) ₆ B ₁₂ H ₁₂	R3	1625.36(7)	9.2319(2)		22.0212(7)		52
<i>m</i> -Fe(MeOH) ₃ B ₁₂ H ₁₂	Cc	1592.3(1)	14.6902(2)	12.6387(3)	8.7958(2)	102.831(1)	190

Table 1. Cont.

Compound	SG	V (Å ³)	a (Å)	b (Å)	c (Å)	β (°)	T (°C)
<i>m</i> -Fe(MeOH)B ₁₂ H ₁₂	<i>P</i> 2 ₁ / <i>c</i>	1223.8(1)	11.7801(6)	8.4249(4)	13.4989(6)	114.011(3)	213
<i>r</i> -FeB ₁₂ H ₁₂	<i>R</i> 3	707.6(4)	10.964(1)		6.797(3)		217
<i>r</i> -Co(MeOH) ₆ B ₁₂ H ₁₂	<i>R</i> 3	1620.00(3)	9.2162(1)		22.0233(3)		62
<i>m</i> -Co(MeOH) ₃ B ₁₂ H ₁₂	<i>C</i> <i>c</i>	1571.78(7)	14.6265(2)	12.5093(2)	8.7795(2)	101.907(1)	190
<i>r</i> -CoB ₁₂ H ₁₂	<i>R</i> 3	679.6(2)	10.866(1)		6.646(1)		65
<i>r</i> -Ni(MeOH) ₆ B ₁₂ H ₁₂	<i>R</i> 3	1607.4(1)	9.1795(3)		22.027(1)		55
<i>m</i> -Ni(MeOH) ₃ B ₁₂ H ₁₂	<i>C</i> <i>c</i>	1559.6(2)	14.5435(4)	12.4575(4)	8.8212(3)	102.616(2)	190
<i>r</i> -NiB ₁₂ H ₁₂	<i>R</i> 3	680.8(3)	10.881(2)		6.640(2)		225
<i>r</i> -Mg(MeOH) ₆ B ₁₂ H ₁₂	<i>R</i> 3	1619.22(7)	9.2014(2)		22.083(6)		60
<i>m</i> -Mg(MeOH) ₃ B ₁₂ H ₁₂	<i>C</i> <i>c</i>	1589.2(2)	14.6728(3)	12.5671(3)	8.8140(2)	102.096(1)	220

3.2. Crystal Structures by SR-XPD and Ab Initio Calculations

3.2.1. *tg*-M(EtOH)₆(B₁₂H₁₂) (M = Mn, Co, Mg)

The formation of hexa-EtOH *closo*-borates was observed for Mn, Co and Mg. The complex forms probably also for Fe, but its structure is not yet solved. Their crystal structures all contain the octahedral complex M(EtOH)₆²⁺ centered inside a *closo*-borate triangular bipyramid (B₁₂H₁₂)₅ of *hcp* anion packing (Figure 6a). The arrangement of the ions has the topology of the hexagonal BN-b, i.e., the cations are displaced from the tetrahedral site of the ZnS-wurtzite type on the triangular face shared between two tetrahedra.

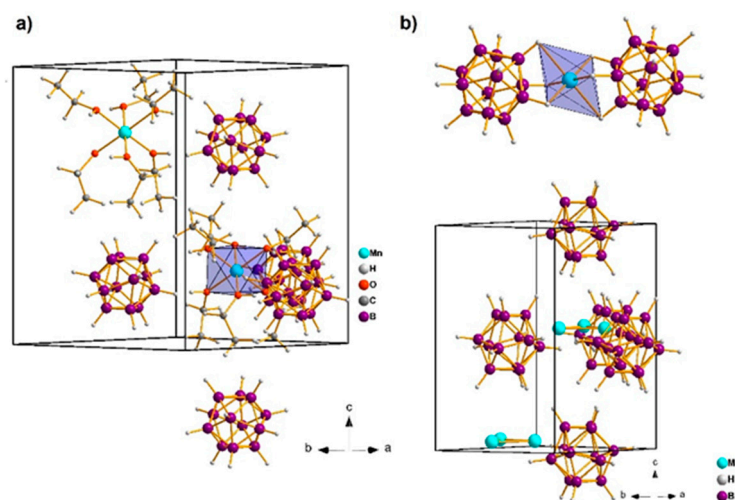


Figure 6. (a) View of the Mn coordination octahedron inside a triangular bipyramid (B₁₂H₁₂)₅ of *hcp* anion packing in *tg*-Mn(EtOH)₆(B₁₂H₁₂) as optimized by density functional theory (DFT). (b) Disordered experimental structure of solvent free *tg*-Mn(B₁₂H₁₂). The metal is disordered inside a triangular bipyramid (B₁₂H₁₂)₅ of *hcp* anion packing. DFT optimized local structure with octahedral coordination of Mn is shown above.

3.2.2. *m*-M(EtOH)₄(B₁₂H₁₂) (M = Co, Ni)

Heating under dynamic vacuum leads in two cases (Co and Ni) to the formation of *closo*-borates *m*-M(EtOH)₄(B₁₂H₁₂) containing square pyramidal complexes with four ethanol and one hydrogen ligands (Figure 7). The complex is located on a triangular face shared between two *closo*-borate tetrahedra (B₁₂H₁₂)₄ of a close to *hcp* anion packing along the *b*-axis.

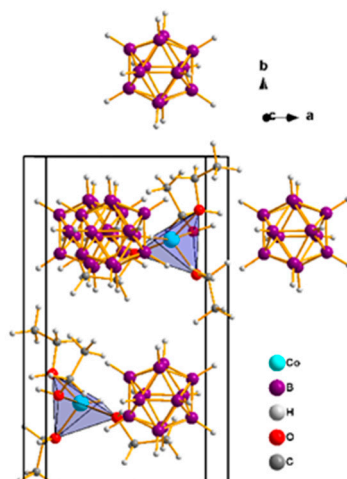


Figure 7. View of the Co coordination square pyramid inside a triangular bipyramid ($B_{12}H_{12}$)₅ of a close to *hcp* anion packing in *m*-Co(EtOH)₄($B_{12}H_{12}$) as optimized by DFT.

3.2.3. *m*-M(EtOH)₃($B_{12}H_{12}$) (M = Mn, Fe, Co, Ni, Mg)

Further heating under dynamic vacuum (for iron also in the closed system) results in a formation of *closo*-borates *m*-M(EtOH)₃($B_{12}H_{12}$) containing metal complexes with three ethanol ligands and two or three hydrogen ligands. The Mn compounds contains a square pyramidal complex Mn(EtOH)₃H₂ centered inside a triangular bipyramid ($B_{12}H_{12}$)₅ of close to *hcp* anion packing, and crystalizing in a monoclinic space group $P2_1/n$ (Figure 8a). The same space group describes the symmetry of Fe, Co, Ni and Mg compounds, but they contain an octahedral Mn(EtOH)₃H₃ complex centered inside a tetrahedron ($B_{12}H_{12}$)₄ of close to *ccp* anion packing (Figure 8b). The change of *closo*-borate packing type from *hcp* to *ccp* thus correlates with the change of coordination polyhedron.

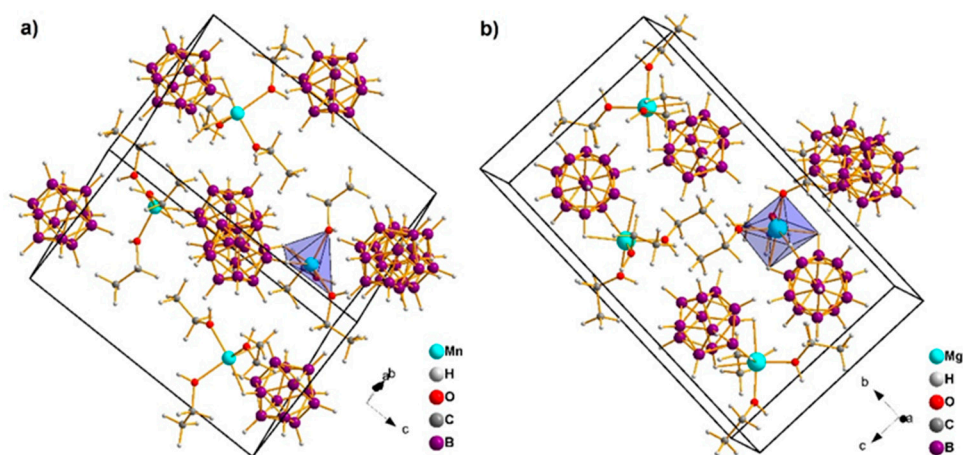


Figure 8. (a) View of the Mn coordination square pyramid inside a triangular bipyramid ($B_{12}H_{12}$)₅ of close to *hcp* anion packing in *m*-Mn(EtOH)₃($B_{12}H_{12}$). (b) View of the Mg coordination octahedron inside a tetrahedron ($B_{12}H_{12}$)₄ of close to *ccp* anion packing in *m*-Mg(EtOH)₃($B_{12}H_{12}$). Both structures optimized by DFT.

While the packing of ions in Mn compound has the wurtzite topology, that of the Fe, Co, Ni and Mg compounds has the topology of the sphalerite.

3.2.4. *m*-Mn(EtOH)₂($B_{12}H_{12}$)•EtOH and *o*-Fe(EtOH)($B_{12}H_{12}$)

By further heating under dynamic vacuum the *closo*-borate *m*-M(EtOH)₃($B_{12}H_{12}$) releases one ethanol molecule from the coordination sphere of Mn, and replaces it by one hydrogen. The released

ethanol molecule stays in the crystal as non-coordinating solvent molecule, and the compound $m\text{-Mn}(\text{EtOH})_2(\text{B}_{12}\text{H}_{12})\cdot\text{EtOH}$ is formed. It contains a square pyramidal complex $\text{Mn}(\text{EtOH})_2\text{H}_3$ bridging two *closo*-borate anions and forming zig-zag chains along the *b*-axis (Figure 9a). The *closo*-borate anions are packed in pseudo-hexagonal layers perpendicular to *c*-axis forming deformed rhombic-prisms $(\text{B}_{12}\text{H}_{12})_8$ containing ethanol molecules.

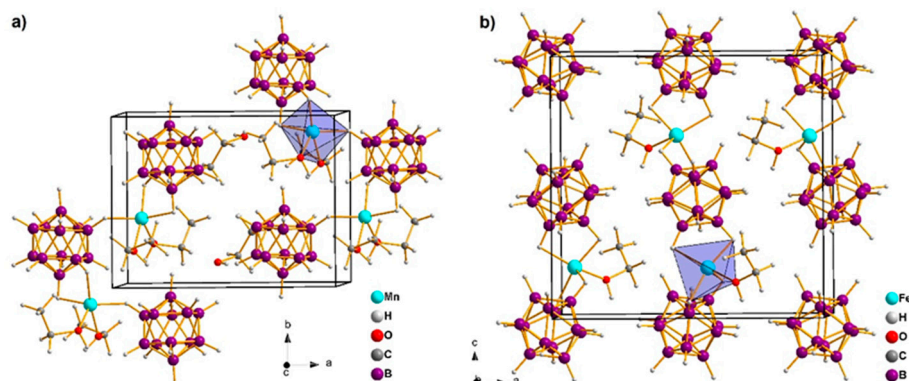


Figure 9. (a) View of the Mn coordination square pyramid bridging two *closo*-borate anions in $m\text{-Mn}(\text{EtOH})_2(\text{B}_{12}\text{H}_{12})\cdot\text{EtOH}$, and forming zig-zag chains along the *b*-axis. Only upper half of the unit cell ($0.5 < z < 1$) is shown for clarity. The *closo*-borate anions are packed in pseudo-hexagonal layers perpendicular to *c*-axis forming deformed rhombic-prisms $(\text{B}_{12}\text{H}_{12})_8$ containing ethanol molecules. (b) View of the Fe coordination triangular bipyramid bridging two *closo*-borate anions in $o\text{-Fe}(\text{EtOH})(\text{B}_{12}\text{H}_{12})$, and forming chains along the *c*-axis. The *closo*-borate anions are packed in nearly regular square layers perpendicular to *b*-axis forming cubes $(\text{B}_{12}\text{H}_{12})_8$ containing ethanol molecules. Both structures optimized by DFT.

In the case of iron, the *closo*-borate $m\text{-Fe}(\text{EtOH})_3(\text{B}_{12}\text{H}_{12})$ releases two ethanol molecules, and the coordination polyhedron changes from the octahedron $\text{Fe}(\text{EtOH})_3\text{H}_3$ to a triangular bipyramid $\text{Fe}(\text{EtOH})\text{H}_4$ in $o\text{-Fe}(\text{EtOH})(\text{B}_{12}\text{H}_{12})$. The complex is also bridging two *closo*-borate anions and forming chains along the *c*-axis (Figure 9b). The *closo*-borate anions are packed in nearly regular square layers perpendicular to *b*-axis forming cubes $(\text{B}_{12}\text{H}_{12})_8$ containing ethanol molecules. Please, note that the experimental structure has contained the EtOH molecule as non-coordinating one, but the DFT optimization of the experimental structure moved the EtOH molecule in the coordination sphere of the iron.

Both structures, $m\text{-Mn}(\text{EtOH})_2(\text{B}_{12}\text{H}_{12})\cdot\text{EtOH}$ and $o\text{-Fe}(\text{EtOH})(\text{B}_{12}\text{H}_{12})$ have the **pcu** topology of anion packing, and CsCl as a structural prototype.

3.2.5. $r\text{-M}(\text{MeOH})_6(\text{B}_{12}\text{H}_{12})$ (M = Fe, Co, Ni, Mg)

Formation of the *closo*-borates containing the metal complex with six methanol ligands was observed for all studied metals, i.e., Fe, Co, Ni and Mg, with the exception of Mn where the structure of the compound in as prepared sample is not yet solved. The crystal structures are identical, and are based on the octahedral complex $\text{M}(\text{MeOH})_6^{2+}$ centered in a *closo*-borate octahedron $(\text{B}_{12}\text{H}_{12})_6$ of *ccp* anion packing (Figure 10a). The arrangement of the ions has the topology of the rock salt.

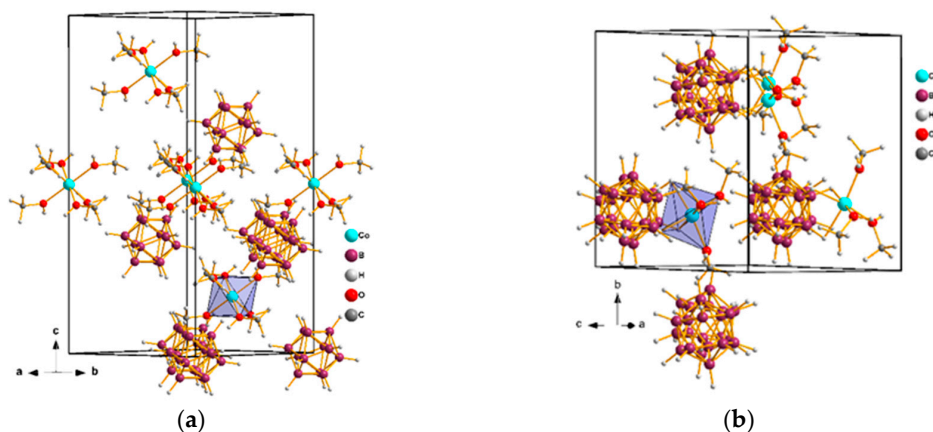


Figure 10. (a) View of the Co coordination octahedron inside an octahedron (B₁₂H₁₂)₆ of *ccp* anion packing as observed in *r*-M(MeOH)₆(B₁₂H₁₂) (M = Fe, Co, Ni, Mg). (b) View of the Co coordination octahedron inside an irregular rhombic-prism (B₁₂H₁₂)₈ as observed in *m*-M(MeOH)₃(B₁₂H₁₂) (M = Fe, Co, Ni, Mg). Both optimized by DFT.

3.2.6. *m*-M(MeOH)₃(B₁₂H₁₂) (M = Fe, Co, Ni, Mg)

By heating under dynamic vacuum the hexa-complex releases three MeOH molecules (for magnesium only under dynamic vacuum), and forms *closo*-borate *m*-M(MeOH)₃(B₁₂H₁₂) containing a heteroleptic octahedral hexa-complex M(MeOH)₃H₃²⁺. The complex is located inside an irregular *closo*-borate rhombic-prism (B₁₂H₁₂)₈ of the *aa* stacking of pseudo-hexagonal *closo*-borate layers (Figure 10b) resulting in CsCl as aristotype.

3.2.7. *m*-M(MeOH)(B₁₂H₁₂) (M = Mn, Fe)

By further heating under dynamic vacuum (for Mn sample also in the closed system), the octahedral complex for Mn and the square pyramidal complex for Fe are formed with only one methanol and five or four hydrogen ligands, respectively. The complex is bridging two *closo*-borate anions and forms zig-zag chains along the *b*-axis for Mn (Figure 11a), and straight chains along the *c*-axis for Fe (Figure 11b). *Closo*-borate anions are packed in quite regular *hcp* for Mn sample. The packing of the pseudo-hexagonal layers deviates strongly from *hcp* in the case of Fe.

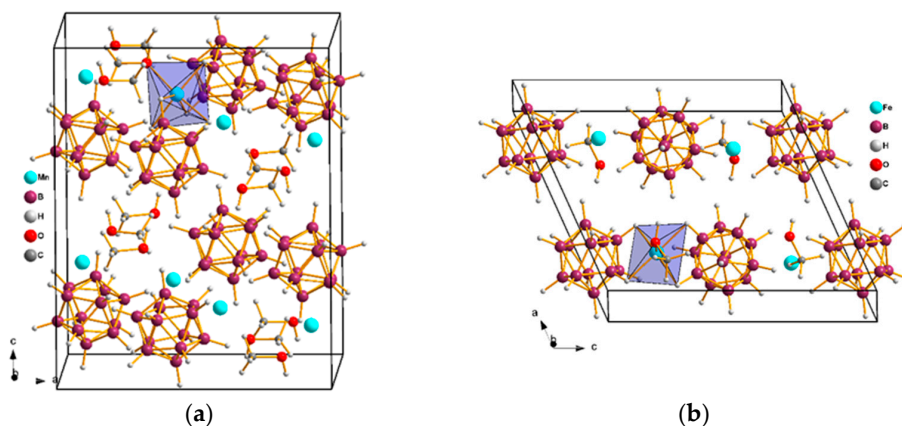


Figure 11. (a) View of the Mn coordination octahedron M(MeOH)₅ bridging two *closo*-borate anions in *o*-Mn(MeOH)(B₁₂H₁₂), and forming zig-zag chains along the *b*-axis. The *closo*-borate anions are packed in pseudo-hexagonal layers perpendicular to *b*-axis and forming nearly regular *hcp*. (b) View of the Fe coordination square pyramid M(MeOH)₄ in *m*-Fe(MeOH)(B₁₂H₁₂) forming straight chains along the *c*-axis. The *closo*-borate packing deviates strongly from *hcp*. Both structures as optimized by DFT.

3.2.8. Solvent-free $M(B_{12}H_{12})$ ($M = Mn, Fe, Co, Ni$)

The solvent-free *closo*-borate forms by further heating under dynamic vacuum only for manganese and cobalt and ethanol synthesis, and for nickel and iron in methanol synthesis. Its formation was hindered in the ethanol synthesis for iron and nickel samples by formation of ternary chlorides, and in the case of magnesium in both syntheses by melting of the sample. The Fe^{2+} , Co^{2+} and Ni^{2+} borates are isostructural, and crystallize with *bcc* packing of anions as well as the disordered Cu^+ borate [22]. On the contrary, the disordered *tg*- $Mn(B_{12}H_{12})$ crystallizes in a trigonal structure with close to *hcp* anion packing (Figure 6b). The octahedral complex MnH_6 is located inside a triangular bipyramid $(B_{12}H_{12})_6$ in a similar way as in *tg*- $Mn(EtOH)_6(B_{12}H_{12})$ with the topology of hexagonal BN-b (Figure 6a). In the experimental structure, the complex is disordered around the trigonal axis. The DFT modelling with one from the three equivalent positions led to the stable octahedral configuration (insert in Figure 6b). The Mn^{2+} cation is now bridging two *closo*-borate anions, which explains its disordering from the center of the triangular face on three equivalent positions.

4. Discussion

The preparation of solvent free 3d transition metal *closo*-borates was the main target of this project in a view of their possible application as insertion electrodes. Solvent free magnesium *closo*-borate is, on the other side, interesting as a possible solid electrolyte conducting Mg^{2+} ions. The former has been achieved by a post-milling solvent addition followed by annealing using any polar protic solvent such as water, ethanol and methanol. Drying under a dynamic vacuum results in a removal of solvent molecules for low boiling point solvents and in a crystallization of solvent free metal *closo*-borates. The NaCl dead mass may be partly removed by filtration using ethanol. All the prepared metal *closo*-borates contain the metal in the lowest oxidation state of (II), which unfortunately prohibits their use as insertion electrodes, as already discussed previously [22]. The attempts of syntheses using halides with a metal in higher oxidation state such as $FeCl_3$ were unsuccessful due to high reducing power of hydroborate. The simple and cheap synthetic procedure unfortunately has not produced magnesium solvent free *closo*-borate.

As already discussed, most of the solvent free 3d TM *closo*-borates crystallize with the *bcc* anionic sublattice. The only exception is *tg*- $Mn(B_{12}H_{12})$ crystallizing with *hcp* anionic sublattice. It may be directly compared to the *closo*-borates of bigger alkali earths such as $SrB_{12}H_{12}$ and $BaB_{12}H_{12}$ where the cation is located in the tetrahedral site [33], and to $CaB_{12}H_{12}$ where smaller cation is located on the triangular face shared by two tetrahedra [34]. Both coordination polyhedra are in agreement with Pauling limits of stability, which are based on the ratio of cation and *closo*-borate anion radii [35]. For even smaller Mn^{2+} this simple calculation predict linear coordination, but is partly hindered by the coordination ability of the transition metal resulting in the coordination octahedron H_6 and Mn^{2+} bridging two *closo*-borates. This leads to a bigger volume per formula unit compared to Ca^{2+} and Sr^{2+} contrary to their ionic radii that are bigger than Mn^{2+} . For Mg^{2+} the ionic radii ratio predict also the linear coordination by two *closo*-borates [33]. The *tg*- $Mn(B_{12}H_{12})$ is therefore a probable model for the long time searched structure of $MgB_{12}H_{12}$. Recent calculations predict $MgB_{12}H_{12}$ structure that is stabilized by the van der Waals attraction between aromatic *closo*-borane anions rather than covalent bond between the metal and $B_{12}H_{12}$ [36].

The coordination of the metal in solvated *closo*-borates has been verified by comparing their volume per formula unit (V/Z). The dependence of the experimental values as a function of number of solvent molecules is presented in the Figure 12. It shows linear behavior similar to that of water solvated *closo*-borates [22]. From the slope of the linear relation, we can obtain the volume per solvent molecule in the crystal. The values of $83(4) \text{ \AA}^3$ for ethanol and $50(1) \text{ \AA}^3$ for methanol are slightly lower than estimated molecules volume in liquid ethanol and methanol at RT of 97 and 67 \AA^3 , respectively [37].

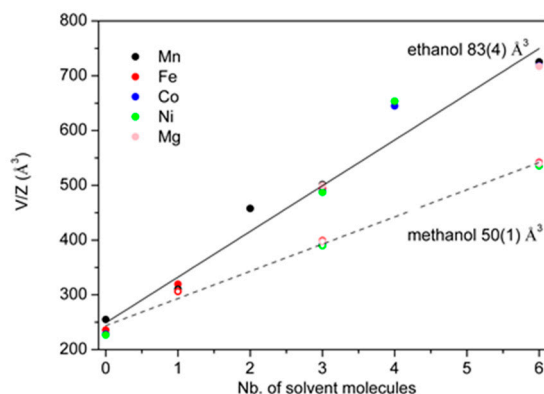


Figure 12. Experimental volume per formula unit (V/Z) as a function of number of ethanol or methanol ligands. The slope of the linear fit gives the average volume per solvent molecule.

To shed more light on the bonding in the solvated metal *closo*-borates, we have calculated Bader charges on complex cations and on metallic centers using the DFT optimized structural models. The charges for octahedral hexa-complexes with water, MeOH and EtOH ligands are presented in the Figure 13a. The charges for other selected *closo*-borates are given in the Figure 13b.

Within the accuracy of the calculations, the positive charge on the whole *hexa*-complex does not change with the metal, i.e., with the number of $3d$ electrons ($\pm 0.02e$ for MeOH and EtOH ligands; $\pm 0.06e$ for H₂O); with increasing number of metal $3d$ -electrons charge of metal decreases. For Mg the charge on the metal is larger than on the whole complex, this means that the charge on octahedral set of ligands is negative. This gives ionic attraction between Mg and ligands, as Mg cannot make orbital hybridization easily and explains higher thermal stability of Mg complexes. Ligands are thus polarized, i.e., have dipole moment that is largest for the case of Mg. An important feature in the optimized structural models is an apparent H⁺ ... H⁻ interaction between the protic hydrogen from the ligand and hydridic hydrogen from the *closo*-borate anion. However, as a main interaction stabilizing the crystal one should consider the ionic interaction between complex cation and complex anion. The H⁺ ... H⁻ interaction then dictates the fine details of the structure.

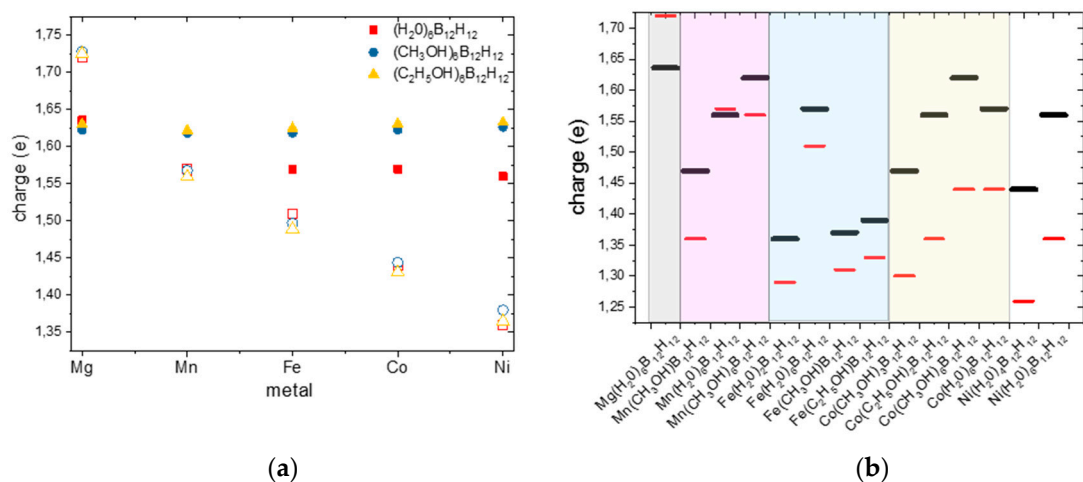


Figure 13. (a) Bader charges on metals (empty symbol) and on the octahedral complex (full symbol) cation with water, ethanol and methanol ligands as a function of valence electrons number. (b) Bader charges on selected complexes as a function of valence electrons number (black line for the entire complex, red line for the metal).

5. Conclusions

The *closo*-borates containing octahedral hexa-complexes $M(\text{EtOH})_6^{2+}$ or $M(\text{MeOH})_6^{2+}$ have been prepared by ball milling of $\text{Na}_2\text{B}_{12}\text{H}_{12} + \text{MCl}_2$ ($M = \text{Mn, Fe, Co, Ni, Mg}$) mixtures followed by ethanol or methanol addition. While the topology of ethanol complexes is that of hexagonal BN-b, the methanol complexes crystallize with rock salt as structural aristotype. The solvent molecules are easily removed by heating under dynamic vacuum leading in some cases to a square pyramidal complex $\text{MH}(\text{EtOH})_4^{2+}$ ($M = \text{Co, Ni}$), and then to square-pyramidal and octahedral complexes $\text{MH}_2(\text{EtOH})_3^{2+}$ ($M = \text{Fe, Co, Ni}$) and $\text{MgH}_3(\text{EtOH})_3^{2+}$, respectively. The octahedral complex $M(\text{MeOH})_3\text{H}_3^{2+}$ forms for ($M = \text{Fe, Co, Ni}$ and Mg) too. In all cases the hydrogen ligands are provided by one *closo*-borate anion $\text{B}_{12}\text{H}_{12}^{2-}$. Further removal of ethanol ligands leads to a square pyramidal complex $\text{Mn}(\text{EtOH})_2\text{H}_3$ bridging two *closo*-borate anions for manganese sample and to a triangular bipyramid $\text{Fe}(\text{EtOH})\text{H}_4$ also bridging two *closo*-borate anions in iron sample. An octahedral complex $\text{Mn}(\text{MeOH})\text{H}_5$ and square pyramidal complex $\text{Fe}(\text{MeOH})\text{H}_4$ bridging two *closo*-borates form by further methanol removal with different topology of anion packing.

Solvent-free *closo*-borate was obtained for Mn, Fe, Co and Ni samples, the first being a probable structural model for not yet synthesized crystalline $\text{Mg}(\text{B}_{12}\text{H}_{12})$. While the anionic network of solvent free *closo*-borates of iron, cobalt, nickel and copper (the last one obtained with water as solvent [22]) has the topology of *bcc* packing, that of the solvent-free $\text{MnB}_{12}\text{H}_{12}$ corresponds to the *hcp* packing of the anions. The Mn^{2+} cations are disordered in the experimental structure around the trigonal axis. The DFT modelling with one from the three equivalent positions led to the stable octahedral complex MnH_6 located inside a triangular bipyramid $(\text{B}_{12}\text{H}_{12})_6$ in a similar way as in $\text{Mn}(\text{EtOH})_6(\text{B}_{12}\text{H}_{12})$ with the topology of wurtzite.

The post-milling addition of a polar protic solvent coordinating the metal followed by annealing has been established as a simple and cheap procedure for crystallization of solvated metal *closo*-borates. Drying in a dynamic vacuum leads to removal of solvent molecules for low boiling point solvents such as water, ethanol and methanol and to crystallization of solvent free metal *closo*-borates.

Supplementary Materials: The following are available online at <http://www.mdpi.com/2073-4352/9/7/372/s1>: Figures S1: IR spectra of *tg*- $\text{Co}(\text{EtOH})_6\text{B}_{12}\text{H}_{12}$ (green line), *RT*- $\text{Fe}(\text{EtOH})_6\text{B}_{12}\text{H}_{12}$ (blue line), *tg*- $\text{Mn}(\text{EtOH})_6\text{B}_{12}\text{H}_{12}$ (red line) and *tg*- $\text{Mg}(\text{EtOH})_6\text{B}_{12}\text{H}_{12}$ (black line) at room temperature; Figure S2: IR spectra of *r*- $\text{Co}(\text{MeOH})_6\text{B}_{12}\text{H}_{12}$ (green line), *r*- $\text{Fe}(\text{MeOH})_6\text{B}_{12}\text{H}_{12}$ (blue line) and *r*- $\text{Ni}(\text{MeOH})_6\text{B}_{12}\text{H}_{12}$ (black line) at room temperature.; Figures S3–S29: Rietveld refinement results and FTIR spectra. Figures S30–S34: Temperature dependent X-ray powder diffraction data. CIF files have been deposited to the database ICSD (FIZ-Karlsruhe) under the numbers CSD 1922595–1922623.

Author Contributions: The manuscript was written through contributions of all authors. All authors have given approval to the final version of the manuscript.

Funding: This research was funded by Swiss National Science Foundation, grant number 200020_172503 and by NCN project 2015/17/B/ST3/02478 and by CPU allocation at PL-Grid.

Acknowledgments: The authors acknowledge the Swiss-Norwegian Beamlines of ESRF for the allocation of beamtime and excellent support with the data collection. Iurii Dovgaliuk (SNBL-ESRF) is acknowledged for data collection of cobalt and nickel *closo*-borate sample. The authors thank Hans Hagemann (University of Geneva) for access to DSC and IR equipment.

Conflicts of Interest: The authors declare no conflict of interest.

References

1. Axtell, J.C.; Saleh, L.M.A.; Qian, E.A.; Wixtrom, A.I.; Spokoiny, A.M. Synthesis and Applications of Perfunctionalized Boron Clusters. *Inorg. Chem.* **2018**, *57*, 2333–2350. [[CrossRef](#)] [[PubMed](#)]
2. Jung, D.; Saleh, L.M.A.; Berkson, Z.J.; El-Kady, M.F.; Hwang, J.Y.; Mohamed, N.; Wixtrom, A.I.; Titarenko, E.; Shao, Y.; McCarthy, K.; et al. A molecular cross-linking approach for hybrid metal oxides. *Nat. Mater.* **2018**, *17*, 341–348. [[CrossRef](#)] [[PubMed](#)]
3. Muetterties, E.L.; Balthis, J.H.; Chia, Y.T.; Knoth, W.H.; Miller, H.C. Chemistry of Boranes. VIII. Salts and Acids of $\text{B}_{10}\text{H}_{10}^{2-}$ and $\text{B}_{12}\text{H}_{12}^{2-}$. *Inorg. Chem.* **1964**, *3*, 444–451. [[CrossRef](#)]

4. Paskevicius, M.; Hansen, B.R.S.; Jørgensen, M.; Richter, B.; Jensen, T.R. Multifunctionality of silver closo-boranes. *Nat. Commun.* **2017**, *8*, 15136. [CrossRef] [PubMed]
5. Tiritiris, I.; Van, N.-D.; Schleid, T. Synthesis and Crystal Structure of $[\text{Ni}(\text{H}_2\text{O})_6][\text{B}_{12}\text{H}_{12}]_6\text{H}_2\text{O}$. *Z. Anorg. Allg. Chem.* **2004**, *630*, 1763. [CrossRef]
6. Tiritiris, I.; Schleid, T. On the Crystal Structures of the Transition-Metal(II)Dodecahydro-closo-DodecaborateHydrates $\text{Cu}(\text{H}_2\text{O})_{5.5}[\text{B}_{12}\text{H}_{12}]_{2.5}\text{H}_2\text{O}$ and $\text{Zn}(\text{H}_2\text{O})_6[\text{B}_{12}\text{H}_{12}]_6\text{H}_2\text{O}$. *Z. Anorg. Allg. Chem.* **2008**, *634*, 317–324. [CrossRef]
7. Van, N.-D.; Kleeberg, F.M.; Schleid, T. Syntheses, Crystal Structures, and Properties of the Isotypic Pair $[\text{Cr}(\text{H}_2\text{O})_6]_2[\text{B}_{12}\text{H}_{12}]_3\cdot^{15}\text{H}_2\text{O}$ and $[\text{In}(\text{H}_2\text{O})_6]_2[\text{B}_{12}\text{H}_{12}]_3\cdot^{15}\text{H}_2\text{O}$. *Z. Anorg. Allg. Chem.* **2015**, *641*, 2484–2489. [CrossRef]
8. Zimmermann, L.W.; Kleeberg, F.M.; Schleid, T. Synthesis and X-ray Crystallography of Two Lead(II) Decahydro-closo-Decaborate Hydrates. *Z. Anorg. Allg. Chem.* **2017**, *643*, 365–372. [CrossRef]
9. Hansen, B.R.S.; Paskevicius, M.; Li, H.-W.; Akiba, E.; Jensen, T.R. Metal boranes: Progress and applications. *Coord. Chem. Rev.* **2016**, *323*, 60–70. [CrossRef]
10. Tiritiris, I.; Schleid, T. Synthese und Kristallstruktur von Cadmium-Dodecahydro-closo-Dodekaborat-Hexahydrat, $\text{Cd}(\text{H}_2\text{O})_6[\text{B}_{12}\text{H}_{12}]$. *Z. Anorg. Allg. Chem.* **2005**, *631*, 1593–1596. [CrossRef]
11. Nguyen-Duc, V. New Salt-Like Dodecahydro-Closo-Dodecaborates and Efforts for the Partial Hydroxylation of $[\text{B}_{12}\text{H}_{12}]^{2-}$ Anions. Ph.D. Thesis, University of Stuttgart, Stuttgart, Germany, 2009.
12. Sivaev, I.B.; Bregadze, V.I.; Sjöberg, S. Chemistry of closo-Dodecaborate Anion $[\text{B}_{12}\text{H}_{12}]^{2-}$: A Review. *Collect. Czechoslov. Chem. Commun.* **2002**, *67*, 679–727. [CrossRef]
13. Udovic, T.J.; Matsuo, M.; Unemoto, A.; Verdal, N.; Stavila, V.; Skripov, A.V.; Rush, J.J.; Takamura, H.; Orimo, S.-I. Sodium superionic conduction in $\text{Na}_2\text{B}_{12}\text{H}_{12}$. *Chem. Commun.* **2014**, *50*, 3750–3752. [CrossRef] [PubMed]
14. Sadikin, Y.; Schouwink, P.; Brighi, M.; Łodziana, Z.; Černý, R. Modified Anion Packing of $\text{Na}_2\text{B}_{12}\text{H}_{12}$ in Close to Room Temperature Superionic Conductors. *Inorg. Chem.* **2017**, *56*, 5006–5016. [CrossRef] [PubMed]
15. Udovic, T.J.; Matsuo, M.; Tang, W.S.; Wu, H.; Stavila, V.; Soloninin, A.V.; Skoryunov, R.V.; Babanova, O.A.; Skripov, A.V.; Rush, J.J.; et al. Exceptional Superionic Conductivity in Disordered Sodium Decahydro-closo-decaborate. *Adv. Mater.* **2014**, *26*, 7622–7626. [CrossRef] [PubMed]
16. He, L.; Li, H.-W.; Nakajima, H.; Tumanov, N.; Filinchuk, Y.; Hwang, S.-J.; Sharma, M.; Hagemann, H.; Akiba, E. Synthesis of a Bimetallic Dodecaborate $\text{LiNaB}_{12}\text{H}_{12}$ with Outstanding Superionic Conductivity. *Chem. Mater.* **2015**, *27*, 5483–5486. [CrossRef]
17. Verdal, N.; Her, J.-H.; Stavila, V.; Soloninin, A.V.; Babanova, O.A.; Skripov, A.V.; Udovic, T.J.; Rush, J.J. Complex high-temperature phase transitions in $\text{Li}_2\text{B}_{12}\text{H}_{12}$ and $\text{Na}_2\text{B}_{12}\text{H}_{12}$. *J. Solid State Chem.* **2014**, *212*, 81–91. [CrossRef]
18. Duchêne, L.; Kühnel, R.-S.; Rentsch, D.; Remhof, A.; Hagemann, H.; Battaglia, C. A highly stable sodium solid-state electrolyte based on a dodeca/deca-borate equimolar mixture. *Chem. Commun.* **2017**, *53*, 4195–4198. [CrossRef]
19. Brighi, M.; Murgia, F.; Łodziana, Z.; Schouwink, P.; Wołczyk, A.; Černý, R. A mixed anion hydroborate/carba-hydroborate as a room temperature Na-ion solid electrolyte. *J. Power Sources* **2018**, *404*, 7–12. [CrossRef]
20. Sadikin, Y.; Didelot, E.; Łodziana, Z.; Černý, R. Synthesis and crystal structure of solvent-free dodecahydro closo-dodecaborate of nickel, $\text{NiB}_{12}\text{H}_{12}$. *Dalton Trans.* **2018**, *47*, 5843–5849. [CrossRef]
21. Fuquan, W.; Yi, W.; Xiangyun, W. On the Preparation of Disodium Salt of Dodecahydrododecaborate. *Chin. J. Appl. Chem.* **1998**, *15*, 111–112.
22. Didelot, E.; Sadikin, Y.; Łodziana, Z.; Černý, R. Hydrated and anhydrous dodecahydro closo-dodecaborates of 3d transition metals and of magnesium. *Solid State Sci.* **2019**, *90*, 86–94. [CrossRef]
23. Favre-Nicolin, V.; Černý, R. FOX, “Free Objects for Crystallography”: A modular approach to ab initio structure determination from powder diffraction. *J. Appl. Crystallogr.* **2002**, *35*, 734–743. [CrossRef]
24. Coelho, A.A. Whole-profile structure solution from powder diffraction data using simulated annealing. *J. Appl. Crystallogr.* **2000**, *33*, 899–908. [CrossRef]
25. Diamond—Crystal and Molecular Structure Visualization. Crystal Impact. Available online: <http://www.crystalimpact.com/diamond> (accessed on 25 April 2019).
26. Spek, A.L. Structure validation in chemical crystallography. *Acta Crystallogr. Sect. D Biol. Crystallogr.* **2009**, *65*, 148–155. [CrossRef]

27. Kresse, G.; Furthmüller, J. Efficient iterative schemes for ab initio total-energy calculations using a plane-wave basis set. *Phys. Rev. B* **1996**, *54*, 11169–11186. [[CrossRef](#)]
28. Kresse, G.; Joubert, D. From ultrasoft pseudopotentials to the projector augmented-wave method. *Phys. Rev. B* **1999**, *59*, 1758–1775. [[CrossRef](#)]
29. Perdew, J.P.; Burke, K.; Ernzerhof, M. Generalized Gradient Approximation Made Simple. *Phys. Rev. Lett.* **1996**, *77*, 3865–3868. [[CrossRef](#)]
30. Dion, M.; Rydberg, H.; Schröder, E.; Langreth, D.C.; Lundqvist, B.I. Van der Waals Density Functional for General Geometries. *Phys. Rev. Lett.* **2004**, *92*, 246401. [[CrossRef](#)]
31. Dudarev, S.L.; Botton, G.A.; Savrasov, S.Y.; Humphreys, C.J.; Sutton, A.P. Electron-energy-loss spectra and the structural stability of nickel oxide: An LSDA+U study. *Phys. Rev. B* **1998**, *57*, 1505–1509. [[CrossRef](#)]
32. Henkelman, G.; Arnaldsson, A.; Jonsson, H. A fast and robust algorithm for Bader decomposition of charge density. *Comput. Mater. Sci.* **2006**, *36*, 354–360. [[CrossRef](#)]
33. Her, J.-H.; Wu, H.; Verdal, N.; Zhou, W.; Stavila, V.; Udovic, T.J. Structures of the strontium and barium dodecahydro-closo-dodecaborates. *J. Alloys Compd.* **2012**, *514*, 71–75. [[CrossRef](#)]
34. Stavila, V.; Zhou, W.; Kim, C.; Ottley, L.A.M.; Udovic, T.J.; Her, J.-H.; Hwang, S.-J.; Her, J.; Hwang, S. ChemInform Abstract: Probing the Structure, Stability and Hydrogen Storage Properties of Calcium Dodecahydro-closo-dodecaborate. *ChemInform* **2010**, *41*, 1133–1140. [[CrossRef](#)]
35. Pauling, L. The principles determining the structure of complex ionic crystals. *J. Am. Chem. Soc.* **1929**, *51*, 1010–1026. [[CrossRef](#)]
36. Maniadaki, A.E.; Łodziana, Z. Theoretical description of alkali metal closo-boranes—Towards the crystal structure of MgB₁₂H₁₂. *Phys. Chem. Chem. Phys.* **2018**, *20*, 30140–30149. [[CrossRef](#)]
37. *CRC Handbook of Chemistry and Physics*, 92nd ed.; DVD Version 2012; CPC Press: Boca Raton, FL, USA, 2011; pp. 3–246.



© 2019 by the authors. Licensee MDPI, Basel, Switzerland. This article is an open access article distributed under the terms and conditions of the Creative Commons Attribution (CC BY) license (<http://creativecommons.org/licenses/by/4.0/>).